Measuring violations of general relativity from single gravitational wave detection by nonspinning binary systems: Higher-order asymptotic analysis

Rhondale Tso[1,2,3,*] and Michele Zanolin[3,†]

[1]*LIGO Laboratory, California Institute of Technology, Pasadena, California 91125, USA*
[2]*Columbia Astrophysics Laboratory, Columbia University, New York, New York 10027, USA*
[3]*Physics Department, Embry-Riddle Aeronautical University, Prescott, Arizona 86301, USA*

(Received 9 September 2015; published 13 June 2016)

A frequentist asymptotic expansion method for error estimation is employed for a network of gravitational wave detectors to assess the amount of information that can be extracted from gravitational wave observations. Mathematically we derive lower bounds in the errors that any parameter estimator will have in the absence of prior knowledge to distinguish between the post-Einsteinian (ppE) description of coalescing binary systems and that of general relativity. When such errors are smaller than the parameter value, there is a possibility to detect these violations from general relativity (GR). A parameter space with inclusion of dominant dephasing ppE parameters (β, b) is used for a study of first- and second-order (co) variance expansions, focusing on the inspiral stage of a nonspinning binary system of zero eccentricity detectible through Advanced LIGO and Advanced Virgo. Our procedure is an improvement of the Cramér-Rao lower bound. When Bayesian errors are lower than our bound it means that they depend critically on the priors. The analysis indicates the possibility of constraining deviations from GR in inspiral signal-to-noise ratio (SNR) ($\rho \sim 15$–17) regimes that are achievable in upcoming scientific runs (GW150914 had an inspiral SNR ~ 12). The errors on β also increase errors of other parameters such as the chirp mass $\mathcal{M}$ and symmetric mass ratio η. Application is done to existing alternative theories of gravity, which include modified dispersion relation of the waveform; nonspinning models of quadratic modified gravity; and dipole gravitational radiation (i.e., Brans-Dicke-type) modifications.

DOI: 10.1103/PhysRevD.93.124033

I. INTRODUCTION

The advanced generation of the LIGO-Virgo network of interferometers [1–3] started collecting data in September 2015 and provided the first detection of gravitational waves (GWs) [4], allowing us to start testing general relativity (GR) beyond current constraints [5] into strongly relativistic regimes [6–8]. In this paper we quantify the capability of laser interferometers to detect violations of GR, with a single detection of a compact binary coalescence signal, by assessing if the minimal error on the parametrized post-Einsteinian (ppE) parameters are larger than the separation of modified gravity values with respect to standard GR values. Error bounds are computed with the most accurate frequentist approach to date by computing the errors as inverse power series in the signal-to-noise ratio (SNR), where the first order is the inverse of the Fisher information matrix [9–11]. In this paper we model GR violations with the ppE framework [8,12–15], which produces parametrized extensions of GR GW signals for the inspiral phase only of a binary compact coalescence in the absence of spin (similar extensions are currently not available for the merger and ringdown phase as well as in the presence of spin).

The square root of the inverse Fisher matrix diagonal elements, also known as the Cramér-Rao lower bound (CRLB), is a lower limit in the error of any unbiased estimator in the absence of prior knowledge. In this regard the CRLB is a statement about the amount of information available in the data regardless of the specific parameter estimation scheme. There is however no guarantee that any estimator is capable of actually attaining the CRLB for part or the whole range of values that the physical parameters can assume. Also, the CRLB only takes into account the curvature of the probability distribution of the data around the true value of the parameters and therefore does not include the role of secondary maxima in the calculation of the variance or mean-squared error of the estimators. The improved bound adopted here (based on second-order asymptotics) is larger than the inverse Fisher matrices, known to underestimate errors in low-SNR detections. Second-order bounds have been previously used for compact binary coalescence waveforms in quantifying the accuracy in intrinsic parameters as well as the direction of arrival for a network of laser interferometers [9–11].

The benefit of using the second order of the expansions is in the fact that they depend up to the fourth derivative on the likelihood function and, therefore, are sensitive to asymmetries and side lobes of the estimator probability distribution (similar to the change in the accuracy of a

*rtso@ligo.caltech.edu
†zanolin@ligo.mit.edu

 © 2016 American Physical Society

Taylor expansion when extended to higher orders). Also, in the past [9–11], the comparison of the second order with the first order provided an analytical understanding of the reasons the CRLB could not be met (for example, in Ref. [10], a novel relationship between the kurtosis of the probability distribution of the estimator and the SNR was derived to understand when the CRLB could be met).

Bayesian methods were recently applied to test modified GR signals through consistency tests [16,17] and the ppE framework [18]. References [16,17] developed a framework to detect GR violations without modeling the violation; this works in the limit of a large number of detections. This framework was used in GR tests from the GW150914 transient [6]. Bayesian selection methods were also used in Refs. [18] and [19] to constrain the range of ppE parameter values, provided that priors are adopted.

When Bayesian uncertainties are smaller than the frequentist bounds, it means that the parameter estimation errors depend critically on the priors. This issue can be an artifact if the prior is not based on previous detections or no robustness studies were performed with respect to the choice of the priors (see, for example, the discussion in Ref. [20] about the effects of priors). In this paper, we show that this instance happens for an equal-mass binary black hole system in the massive graviton case. This example illustrates how the present work provides a unique understanding of the parameter estimation errors. Although GW150914 had a SNR ~ 24, its inspiral stage falls within the prescribed study of SNR < 20.[1]

In addition, this work extends the Fisher-information-based results of Refs. [13–15], which perform error estimations by modifying post-Newtonian (PN) coefficients. We also extend Fisher-based assessments of specific alternative theories [21–25]. Specifically, this paper considers phase modification in the *restricted* ppE framework [8], considering the ppE framework as a general enhancement to existing `TaylorF2` [26,27] GR templates in a three-detector LIGO-Virgo network [1–3]. Calculations in this limit were chosen since deformations to the GW's phase are expected to be more resolvable [18,28] and complement recent Bayesian methods testing deviations from GR [16,17]. Second-order frequentist constraints produced in this paper are at the same order of magnitude as the Bayesian model selection's errors in Ref. [18], where our errors are quantified at the one sigma level. As error estimates of ppE parameters grow, second-order errors of parameters such as the chirp mass, symmetric mass ratio, and time of coalescence also inflate. The results presented here, and the rescaled bonds, which can be simply derived by changing the SNR, will be important benchmarks for any parameter estimation scheme that will be used in existing and future interferometer data, including Bayesian parameter estimation algorithms.

[1]GW150914 has inspiral SNR ~ 12.

Section I A of this paper introduces the signal model used. Section II discusses the resolvable parameter space and the expansion model; in particular, Sec. II A discusses alternative theories of gravity covered in this paper, and the asymptotic expansion of the maximum likelihood estimator model is discussed in Sec. II B. Finally, Sec. III assesses the results, as applied to a two-dimensional ppE parameter space (Sec. III A) and a seven-dimensional parameter space of equal-mass (Sec. III B) and unequal-mass (Sec. III C) systems with physical parameters included. Results are applied to existing alternative theories of gravity in Sec. III D, including massive graviton, Brans-Dicke, and quadratic modified gravity (encompassing Einstein-dilation-Gauss-Bonnet gravity). A summary and discussion is given in Sec. IV.

A. Signal model

The waveforms are assumed to be produced by a nonspinning binary system with all orbital eccentricity information lost when entering the frequency bandwidth of Advanced LIGO and Advanced Virgo. The Fourier transform of the signal, through the stationary phase [29,30], becomes

$$s^I_{\rm GR}(f) = A^I_{\rm GR}(f) e^{i(\psi_{\rm GR}(f) - 2\pi f \tau_I - \Phi^I_0)}, \qquad f < f_{\rm merg} \tag{1.1}$$

for the inspiral stage of the compact binaries. For the phase $\psi_{\rm GR}(f)$ and amplitude $A^I_{\rm GR}(f)$, the standard `TaylorF2` model [26,27] is used.

The signal of a collection of alternative theories of gravity is modeled as (1.1) modulated in the phase and amplitude as

$$\begin{aligned} A^I_{\rm GR}(f) &\to A^I_{\rm GR}(f)(1 + \delta A(f)), \\ \psi_{\rm GR}(f) &\to \psi_{\rm GR}(f) + \delta\psi(f), \end{aligned} \tag{1.2}$$

where $\delta A(f)$ and $\delta\psi(f)$ are a general series of scaling parameters $\alpha_i, \beta_i \in \Re$, and in some instances arguments call for integer exponentials of $\nu\eta^{1/5}$ [31,32], where $\nu = (\pi M f)^{1/3}$ for total mass M and $\eta = m_1 m_2/M^2$. Here the analysis is done at leading order in the ppE parameters,

$$\begin{aligned} \delta A_{\rm ppE}(f) &= \alpha(\nu\eta^{1/5})^a, \\ \delta\psi_{\rm ppE}(f) &= \beta(\nu\eta^{1/5})^b. \end{aligned} \tag{1.3}$$

At each interferometer the signal is assumed to be recorded with additive noise as in Ref. [11]. Frequency-dependent noise for Advanced LIGO is interpolated from the official power spectral density [33] of high power, zero detuning. Advanced Virgo is assumed to have the sensitivity given in Ref. [34]. For error analysis, and upcoming integrations, the lower cutoff frequency is set to $f_{\rm low}$ and the upper cutoff is set to the upper limit for reliability in the inspiral of the waveform template, i.e., the innermost stable circular orbit (ISCO) frequency,

$$f_{\rm low} = 20\ {\rm Hz}, \qquad f_{\rm up} = f_{\rm ISCO} \approx (6^{3/2}\pi M)^{-1}.$$

The convention used in (1.1) is presented in the Appendix.

II. PARAMETER SPACE AND EXPANSION

For nonspinning systems 13 parameters are necessary in the description of the inspiral of two coalescing binaries: two mass terms, four angles (two source location and two waveform angles), two coalescence parameters, distance to the source, and four ppE parameters in the leading-order approximation. Singular Fisher matrices might appear [10,35], indicating that the resolvable parameter space is smaller (where the Fisher matrix approach can still be used).

The distance D_L is excluded from the error estimates because the amplitude has a dependency on both mass and distance parameters, and the independent treatment of both is unresolvable as already indicated in Ref. [11]. The coalescence phase is also not included because estimations of ϕ_c are relevant only when a full waveform (inspiral, merger, and ringdown) is implemented. The polarization ψ is excluded because results tend to be independent of it [11].

Derivatives of the fitting factor (FF) [28],

$$FF = \max_{\vec{\zeta}} \left(\frac{\langle s_1(\vec{\lambda}) | s_2(\vec{\zeta}) \rangle}{\sqrt{\langle s_1(\vec{\lambda}) | s_1(\vec{\lambda}) \rangle} \sqrt{\langle s_2(\vec{\zeta}) | s_2(\vec{\zeta}) \rangle}} \right) \tag{2.1}$$

with respect to the binary's inclination ϵ evaluated at, or in the neighborhood of, $\epsilon = 0$ are roughly zero, leading to the impossibility to estimate ϵ and singular Fisher matrices. Here the $\langle \cdot | \cdot \rangle$ represent noise weighted inner products [11,36] and $s_{1,2}$ are GW signals controlled by general parameter space vectors $\vec{\lambda}$ and $\vec{\zeta}$. Keeping other parameters fixed and varying only ϵ produces change in the SNR equivalent to the rescaling of the distance, which affects GW plus-cross polarizations similarly. The top panel in Fig. 1 shows the sky-averaged SNR plotted as a function of inclination ϵ (only the GR polarizations are considered). Also, sky patterns of the errors remain consistent when varying ϵ. Therefore, since ϵ is degenerate with D_L it is also excluded from our resolvable parameter space, which becomes $\theta^i_{\rm phys} = \{\eta, \log \mathcal{M}, t_c, {\rm lat}, {\rm long}\}$.

Throughout this paper amplitude modulations are to be held fixed to that of GR, $\alpha = 0$, because the same effect could be produced by changing physical parameters like distance or mass. Such an approach supposes that GR-violating amplitudes in the waveform are suppressed or modifications manifest only in waveform propagation.[2]

[2]Modifications to just propagation could surface through alterations in the dispersion of the GW, with alterations stemming from waveform generation excluded [22,25]. Past studies also indicate modulations that are most sensitive to phase modulations [18,28].

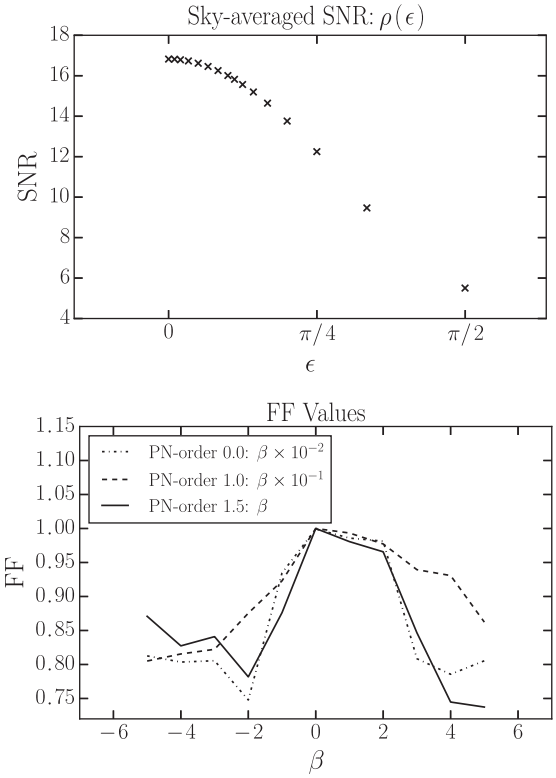

FIG. 1. Top: Sky-averaged SNR plotted with ϵ varied for system parameters: $m_1 = m_2 = 10M_\odot$, $t_a = \phi_a = 0$, $\beta = -0.2$, $D_L = 1100$ Mpc, and $b = -3$ in the three-detector network. Bottom: Fitting factors (2.1) for a range of β with b fixed to produce PN-order 0.0, 1.0, and 1.5 modifications for a system of $m_1 = m_2 = 10M_\odot$ and $t_a = \phi_a = 0$. Advanced LIGO noise is assumed. Since the range of β-values scales differently at each PN order, each β-interval is scaled (as labeled in the legend). For example, in the PN-order 0.0 modification the β values in the domain are each scaled by 10^{-2}.

Also, recent work suggests that GR modifications produced during the generation of a waveform can be disentangled from that produced during propagation [31]; thus, in the event that phase deformation dominates GR-violating effects, amplitude modifications can be disregarded. Calculations in this restricted framework are performed with modifications at various PN orders in the phase, where in the strong-field regime discrete values of b control what PN-order correction is constituted for free parameter β (GR result: $\beta = 0$).

A qualitative way to study the influence of ppE parameters (β, b) on a GR signal can be obtained through the correlation of the signals by means of the fitting factor (2.1). Each integration is done from 20 Hz to $f_{\rm ISCO}$ with the noise curve of Advanced LIGO [33] "high power, zero detuning." Our exact waveform s_1 is represented by a `TaylorF2` waveform, whereas a modified `TaylorF2`, formed through (1.2) and (1.3), acts as s_2. So $\vec{\lambda}$ is the GR-limit parameter space vector and $\vec{\zeta}$ is that of the ppE

parameter space. The inner products are maximized over evenly spaced parameters $\vec{\zeta}$ to provide an FF-value, where $FF = 1$ represents an exact match between signals. Both `TaylorF2` models are kept to PN order 3.5 in the phase. In the denominator of (2.1), amplitude parameters normalize to leave $f^{-7/3}/S_h$ in each integrand. The numerator retains the integrand $(f^{-7/3}/S_h)e^{i\Delta\psi(f;\vec{\lambda},\vec{\zeta})}$, where

$$\Delta\psi(f;\vec{\lambda},\vec{\zeta}) = \psi(f;\vec{\lambda}) - \psi(f;\vec{\zeta}) - \delta\psi_{\rm ppE}(f),$$

and, in fixing b and varying β, the parameters that need to be maximized over are $\vec{\zeta} = \{t_c, \phi_c, \eta, M_{\rm tot}\}$. The parameters are evenly spaced, in a $30 \times 30 \times 30 \times 30$ grid, within intervals: $0.05 \le \eta \le 0.25$, $0.5M_{\rm tot} \le M_{\rm tot} \le 1.5M_{\rm tot}$, $-\pi \le \phi_c \le \pi$, and $-1.3 \times 10^{-2} \le t_c \le 1.3 \times 10^{-2}$.

Figure 1 displays the results for an equal-mass system of $m_1 = m_2 = 10M_\odot$ and $t_a = \phi_a = 0$ for PN-order 0.0, 1.0, and 1.5 modifications in the waveform. Parameters $\vec{\zeta}$ are maximized over for a variety of β-values. Note that at lower PN orders the interval of β is scaled differently than the $-5 \le \beta \le 5$ depicted, an interval valid for PN-order 1.5 modifications. The general trend is that the fitting factor is less affected by β for a larger PN order with a skew in the FF-distribution towards the positive domain of β-values.

A. Restricted ppE template and existing dephasing alternatives

As stated, variations of β are restricted to fixed PN-order corrections in the phase. For the two-dimensional study b is fixed to induce modifications at (separately) PN orders 0.0, 0.5, 1.0, 1.5, 2.0, and 3.0, which acts as a demonstration to the error estimation procedure. Higher-dimensional studies specifically target a PN-order 1.0 modification and a weak-field $b = -7$ modification to address dispersion modification and dipole gravitational radiation. From this reason β is varied with error estimations performed at each β-value. In Ref. [37] an analysis of binary pulsar PSR J0737-3039 [38] placed bounds on ppE parameters (for this binary $4\eta \approx 1$ as determined from radio pulsar measurements [38]). At PN-order 2.5 ($b = 0$) degeneracies occur with other fiducial parameters, thus is not considered in the analysis. In some theories constraints for $b = -7$ cannot be implemented from pulsar measurements, due to β's dependence on mass differences of the system and other theoretical parameters that will be discussed shortly. With the exception of $b = -7$, parameters that probe the weak field ($b < -5$) are not considered since they are better constrained via binary pulsar measurements [18].

At $b = -7$, the even-parity sector of quadratic modified gravity (QMG), an example being Einstein-dilation-Gauss-Bonnet (EDGB) gravity, can be explored. For even-parity QMG, the violating term for a BBH system depends on the mass differences of the BHs: $\beta \propto \zeta_3\eta^{-18/5}(1-4\eta)$, unresolvable for equal-mass systems [39]. For BHNS systems, the violating coefficients depend on the ratio of the two bodies: $\beta \propto \zeta_3\eta^{-8/5}(m_{\rm NS}/m_{\rm BH})^2$ due to the "scalar charge" vanishing in NSs [39,40]. With this same $b = -7$ correction, examples of dipole gravitational radiation, like Brans-Dicke (BD), can also be assessed. Here BD-like modifications further depend on the difference of parameters that measure the body's inertial mass variations with respect to the local background value of the effective gravitational constant. These so-called "sensitivity parameters" $s_{\rm BH,NS}$ are generally set to 0.5 for black holes, so their differences vanish for a BBH system. Only a BHNS system would allow constraints of BD-like modifications since $0.2 \le s_{\rm NS} \le 0.3$ [41–44].

For corrections at $b \neq -7$, most existing modifying coefficients depend on parameters that either vanish in the nonspinning model (1.1) or contribute beyond PN order 3.5. This is the case in specific models of QMG, e.g., the odd-parity sector and dynamical Chern-Simons (CS) gravity [39]. As an example, in the circular inspiral of two comparable mass BHs the GR-deviating term of dynamical CS has dependencies on the BH spins $\hat{S}_{1,2}$ and their relations to their orbital angular momentum $\hat{L}$: $\delta C = \delta C(m_{1,2}, \hat{S}_{1,2}, \hat{L})$ [45]. When the binary system is nonspinning, modifications are beyond PN order 3.5.

Beyond modifications during waveform generation, two propagating effects are massive graviton (MG) and simplified versions of Lorentz-violating (LV) theories [22,25]. The parameters to constrain are the graviton Compton wavelength λ_g and $\lambda_{\rm LV} = 2\pi\mathbb{A}^{1/(\gamma-2)}$. Here $\mathbb{A}$ is a phenomenological parameter modifying the gravitational waveform's dispersion relation. The γ-dependent distance measure D_γ (see Ref. [25] for exact formula) further depends on known astrophysical parameters (Hubble parameter, matter density parameter, etc.), which are assumed to be exact knowns in the analysis [46]. Parameter γ governs the order of correction and $\gamma = 0$ (PN order 1.0) is what we are limited to since this is the only value contained in the ppE framework for the PN-order 3.5 `TaylorF2` model. Such MG-LV interpretations are generic models modifying the dispersion of a GW with a more specific generation mechanism still yet to be explored. Reference [16] notes some limitations in prescribing MG effects as modifications of the dispersion of the waveform. In LV-type modification further work in existing, model-independent approaches, e.g., the Standard Model extension [47,48], could be interesting (see, for example, Ref. [49]).

Constraints have been imposed on the wavelength of the graviton. The detection of GW150914 and the binary-pulsar constraint serve as dynamical bounds while solar-system constraints, serving as static bounds, provide the most reliable estimates [6,50]. So, parameters are represented by

$$\lambda_{\rm LV} = 2\pi\mathbb{A}^{-1/2}, \qquad \lambda_g \geq \begin{cases} 10^{13}\ [\text{km}], & \text{dynamic (GW)}, \\ 1.6\times 10^{10}\ [\text{km}], & \text{dynamic (pulsars)}, \\ 2.8\times 10^{12}\ [\text{km}], & \text{static}. \end{cases}$$

For EDGB gravity, the constraint parameter is $|\alpha_{\rm EDGB}|$. Here $\zeta_3 = \xi_3 M^{-4} = 16\pi\alpha^2_{\rm EDGB}M^{-4}$, with $\beta_{\rm BBH} \propto \zeta_3\eta^{-18/5}(1-4\eta)$ and $\beta_{\rm BHNS} \propto \zeta_3\eta^{-8/5}(m_{\rm NS}/m_{\rm BH})^2$. In Brans-Dicke theory $\beta \propto (s_{\rm BH,NS} - s_{\rm BH,NS})^2\omega_{\rm BD}^{-1}$. From measurements of the Cassini spacecraft [51,52] bounds on EDGB and the Brans-Dicke parameters are

$$|\alpha_{\rm EDGB}|^{1/2} \leq 8.9\times 10^6\ \text{km},$$
$$\omega_{\rm BD} > 4\times 10^4.$$

With other suggested constraints [40,53] giving

$$|\alpha_{\rm EDGB}|^{1/2} < 1.9\ \text{km},$$
$$|\alpha_{\rm EDGB}|^{1/2} < 9.8\ \text{km},$$

GW150914 results have allowed studies to infer the theoretical significance of the testing GR study [6] in various specific models; see, for example, Refs. [54,55].

B. Asymptotic expansions

Similar to Ref. [11], we reasonably assume only Gaussian noise at the time of the signal and that the noise is uncorrelated at different interferometers. Here we use the analytic asymptotic expansion of the variance and bias developed in Refs. [9–11],

$$\sigma^2_{\vartheta^i} = \sigma^2_{\vartheta^i}[1] + \sigma^2_{\vartheta^i}[2] + \cdots, \tag{2.2}$$

$$b_{\vartheta^i} = b_{\vartheta^i}[1] + b_{\vartheta^i}[2] + \cdots, \tag{2.3}$$

with $\sigma^2_{\vartheta^j}$ being the diagonal elements of the covariance matrix, where

$$\sigma_{\vartheta^j}[1], b_{\vartheta^j}[1] \propto \rho^{-1},$$
$$\sigma_{\vartheta^j}[2], b_{\vartheta^j}[2] \propto \rho^{-2},$$

for network SNR ρ. This inverse proportionality continues at higher orders in similar fashion. Here the network SNR is the sum over the square of the optimal SNR ρ^I of the signal at the Ith detector,

$$\rho^2 = \sum_I (\rho^I)^2, \qquad \rho^I = \langle s^I|s^I\rangle^{1/2}. \tag{2.4}$$

Notice that ρ increases for a fixed source by increasing the number of detectors. The first-order term of the expansion of the variance, the diagonal components of the inverse Fisher matrix, dominates the bound on the error in the limit of large SNR, while higher-order terms become more important for medium to low SNR.

What is usually regarded as the error in a lab measurement is the square root of the mean-squared error (MSE), where the MSE is the sum of the variance (2.2) and square of the bias (2.3): $\text{MSE}_{\vartheta^i} = \sigma^2_{\vartheta^i} + b^2_{\vartheta^i}$. Since this analysis computes errors at the second order of $1/\rho$, the expression above only requires the first order of the bias, which is negligible, as already discussed in Ref. [11]. We estimate uncertainties of the two-dimensional ppE parameter space $\theta^i_{\rm ppE}$ for different β at a fixed exponential b. In addition, the inclusion of $\theta^i_{\rm ppE}$ to a signal's extrinsic and intrinsic parameter space $\theta^i_{\rm phys}$ is also assessed.

Finally, error bounds are indicated with

$$\Delta\vartheta_i[1] = \sqrt{\sigma^2_{\vartheta^i}[1]}, \qquad \Delta\vartheta_i[2] = \sqrt{\sigma^2_{\vartheta^i}[2]}$$
$$\Delta\vartheta_i[1+2] = \sqrt{\sigma^2_{\vartheta^i}[1] + \sigma^2_{\vartheta^i}[2]}. \tag{2.5}$$

For example, first-order errors of the symmetric mass ratio η are marked by $\Delta\eta[1]$, second-order errors are marked by $\Delta\eta[2]$, and total error with the inclusion of second-order contributions by $\Delta\eta[1+2]$.

III. RESULTS

In this section we explore the error bounds both as a function of the SNR and sky location of the source. The asymptotic expansion approach is first applied to a two-dimensional ppE parameter space (when the physical parameters are known) of equal-mass systems. Only phase corrections are assumed through unknown ppE parameters (β, b), while b probes modifications at PN orders 0.0–3.0 of the `TaylorF2` model (of a PN-order 3.5 phase). Based on Refs. [9–11] this approach is expected to give overly optimistic errors. The Fisher information error estimates presented here for the ppE parameters are at least an order of magnitude smaller than results with a Bayesian model selection [18].

To identify SNR dependencies and regions of lowest error estimates the sky dependencies of errors are observed through a 289-point sky grid. A point $(\text{lat}_i, \text{long}_j)$ in latitude-longitude coordinates (of the Earth frame) on the sky grid follows from the procedure of Ref. [11] (detector

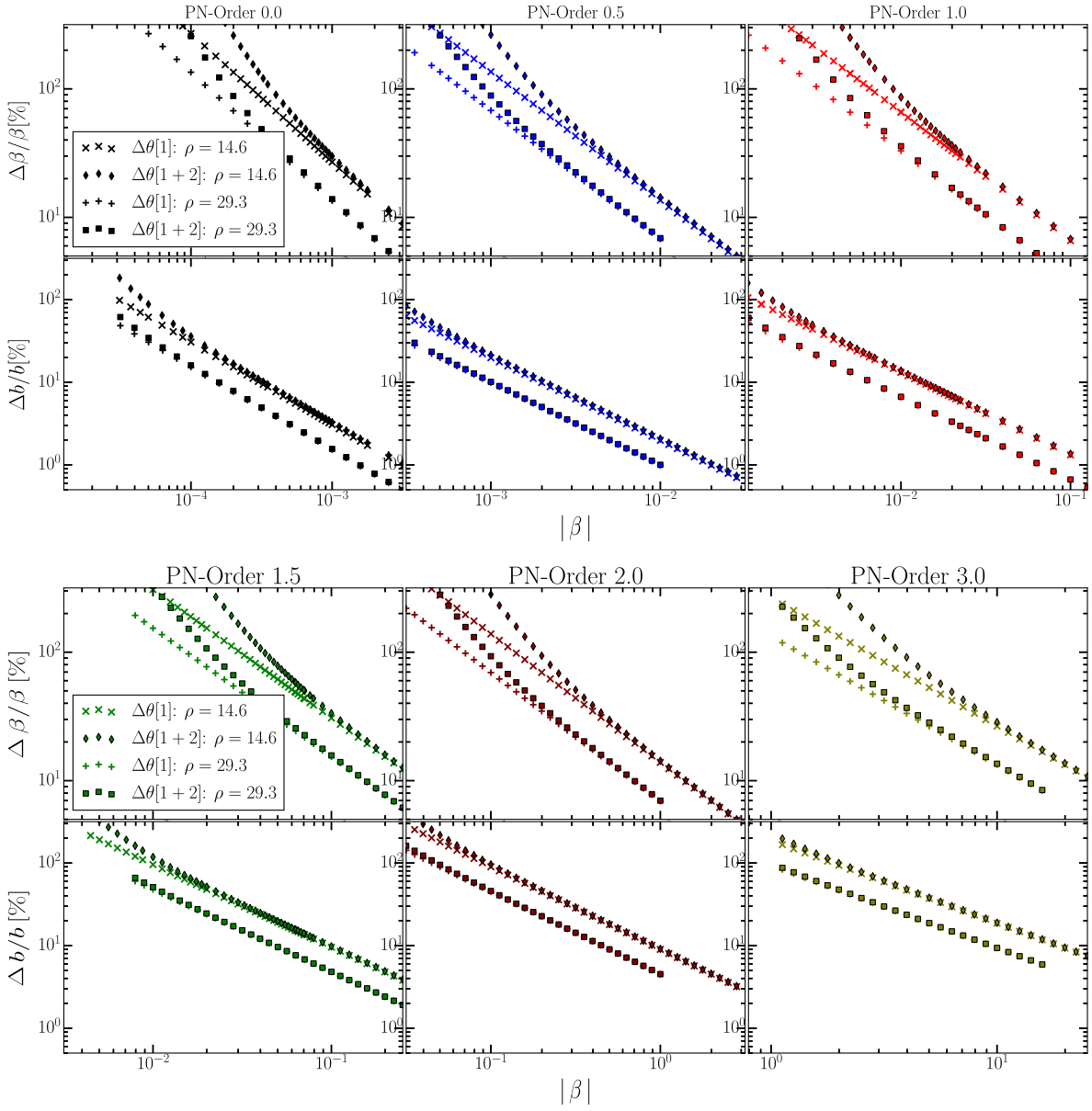

FIG. 2. Sky-averaged errors as a function of β for a two-dimensional ppE parameter space for the BBH 1:1 system of averaged network SNR $\rho = 14.6$. SNR results of $\rho = 29.3$ are also shown by setting the distance to $D_L = 550$ Mpc. As noted in Ref. [11] error estimates are rescaled as $\sigma[1](\rho^*/\rho)$ and $\sigma[2](\rho^*/\rho)^2$, where ρ^* is the SNR that error estimates are originally calculated from. In the top panel the far left column represents each system for a PN-order 0.0 modification ($b = -5$), the center column is a PN-order 0.5 modification ($b = -4$), and the far right column is for PN-order 1.0 modifications ($b = -3$). Similarly, the bottom panels are resulting modifications at PN order 1.5 ($b = -2$), 2.0 ($b = -1$), and 3.0 ($b = +1$). β is more tightly constrained at lower PN orders and the inclusion of second-order errors for (β, b) drastically diverges from Fisher estimates as $\beta \to 0$.

coordinates also follow Ref. [11], which are fixed in the Earth frame as given in Refs. [56,57]).

As discussed in Sec. II, $\epsilon = \pi/6$ is a fixed value and is excluded in error analysis. Parameter ψ is also fixed, and arbitrary values can be chosen for fiducial parameters ϕ_c and t_c. The sky-averaged SNR is restricted to an inspiral phase $\rho < 20$ to focus on the more likely advanced interferometer scenarios. For each system considered, the distance of the resolved signal in the network is varied to keep a fixed SNR. For a three-detector network ($I = H, L, V$) the following is chosen for the equal-mass binary systems:

(i) BBH 1:1: $(m_1, m_2) = (10, 10)M_\odot$, $D_L = 1100$ Mpc,
(ii) BNS: $(m_1, m_2) = (1.4, 1.4)M_\odot$, $D_L = 200$ Mpc.

Here the constructed binary black hole (BBH) and binary neutron star (BNS) system leaves the network with an averaged SNR of $\rho = 14.6$ and $\rho = 17.0$, respectively. For unequal mass systems we choose a BBH system with a 1:2

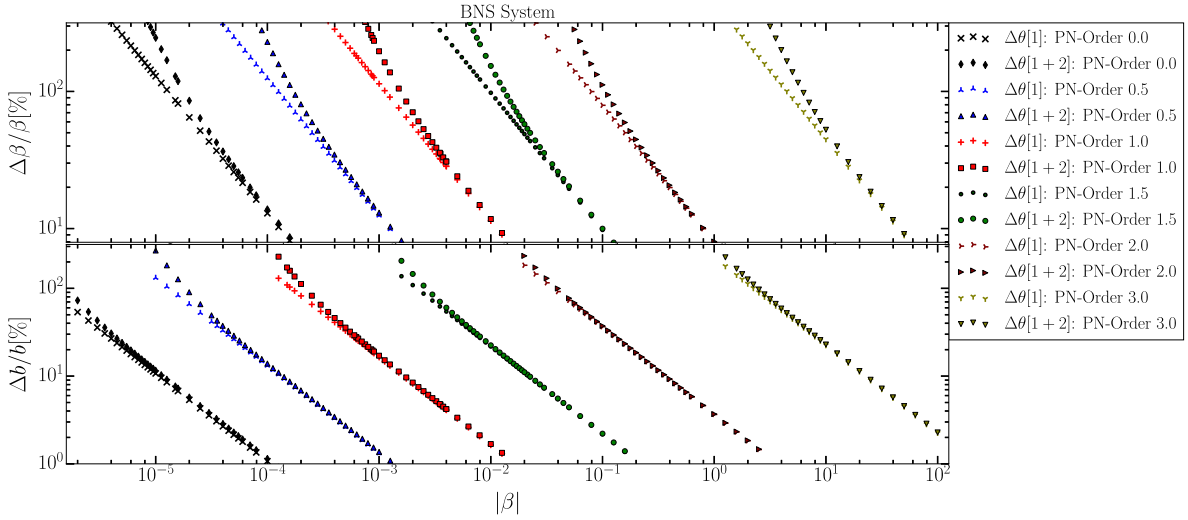

FIG. 3. Sky-averaged errors, similar to Fig. 2, for a BNS system of averaged SNR $\rho = 17.0$.

mass ratio and a black hole–neutron star (BHNS) binary with the following:

(i) BBH 1:2: $(m_1, m_2) = (5, 10)M_\odot$, $D_L = 850$ Mpc,
(ii) BHNS: $(m_1, m_2) = (1.4, 10)M_\odot$, $D_L = 450$ Mpc,

which respectively give SNRs of $\rho = 14.9$ and $\rho = 15.8$. For direction reconstruction and related extrinsic parameters the network geometry is important; however, for intrinsic parameters (as with the ppE parameters) SNR gains and losses have a larger impact [11].

In the seven-dimensional study, β is varied along $b = -3, -7$ for a BBH 1:1, 1:2, and BHNS systems. The reason for $b = -3$ is that it simulates modifications to the dispersion of a GW (e.g., massive gravitons or Lorentz violations [22,25]). Also, $b = -7$ simulates weak-field modifications for dipole gravitational radiation (e.g., Brans-Dicke [8,21]) and the nonspinning, even-parity sector of quadratic modified gravity (e.g., Einstein-dilation-Gauss-Bonnett, or EDGB, gravity [39]). Distinguishability from GR is denoted as the condition that errors are smaller than the separation between parameters of the GR limit and that of some alternative theory.

A. Two-dimensional study: Equal mass

In this subsection uncertainties for a two-dimensional parameter space are computed for both the BBH 1:1 and BNS systems, marked by $\Delta\theta^i_{\rm ppE}$. Parameter b is chosen at a fixed PN-order correction with PN order 0.0, 0.5, 1.0, 1.5, 2.0, and 3.0 (i.e., $b = -5, -4, -3, -2, -1, +1$) while β is varied at each PN order. Here β probes values small enough to induce a sky-averaged error larger than 100% in b and large enough for $\lesssim$10% sky-averaged error in β. Errors for the BBH 1:1 system are depicted in Fig. 2, each labeled column representing a particular PN-order modification. Furthermore, to demonstrate the SNR dependence the BBH 1:1 system contains values for the scenario in which the SNR is doubled; for this the distance is decreased to $D_L = 550$ Mpc. Figure 3 illustrates similar results for the BNS system.

The constant slopes of errors at first order are cataloged in Table I for each PN order. The computed first-order errors are consistent with statements of Ref. [18], which demonstrate that different PN-order corrections lead to different feasible constraints on β-values. BNS systems offer tighter constraints on β at each chosen b. It is interesting to observe that scaling parameters controlling propagating modifications, e.g., the graviton wavelength $\beta_{\rm MG} \propto \lambda_g^{-2}$, are not more tightly constrained with BNS systems at shorter distances than BBH systems at larger distances. Rather, parameters like $\beta_{\rm MG}$ also depend on a distance measure and masses of the compact objects that adversely affect constraints at shorter distances and smaller masses.

The smaller β is, the more second-order effects in the errors contribute. Second-order effects on the errors of b are less significant, and only errors $>100\%$ on β force sizable

TABLE I. Constant slopes of first-order error bound estimates of the BBH 1:1 (for SNR $\rho = 14.6$) and BHNS systems for all β values. Here percent errors [%] follow a $1/\beta$ relationship for $\Delta\beta[1]$ represented above for respective PN orders.

Error bounds (system)	PN order 0.0	PN order 0.5	PN order 1.0	PN order 1.5	PN order 2.0	PN order 3.0
$\Delta\beta[1]$ (BBH 1:1)	2.70×10^{-4}	1.36×10^{-3}	6.59×10^{-3}	3.07×10^{-2}	1.39×10^{-1}	2.66
$\Delta\beta[1]$ (BNS)	1.29×10^{-5}	1.24×10^{-4}	1.14×10^{-3}	9.78×10^{-3}	7.93×10^{-2}	4.49

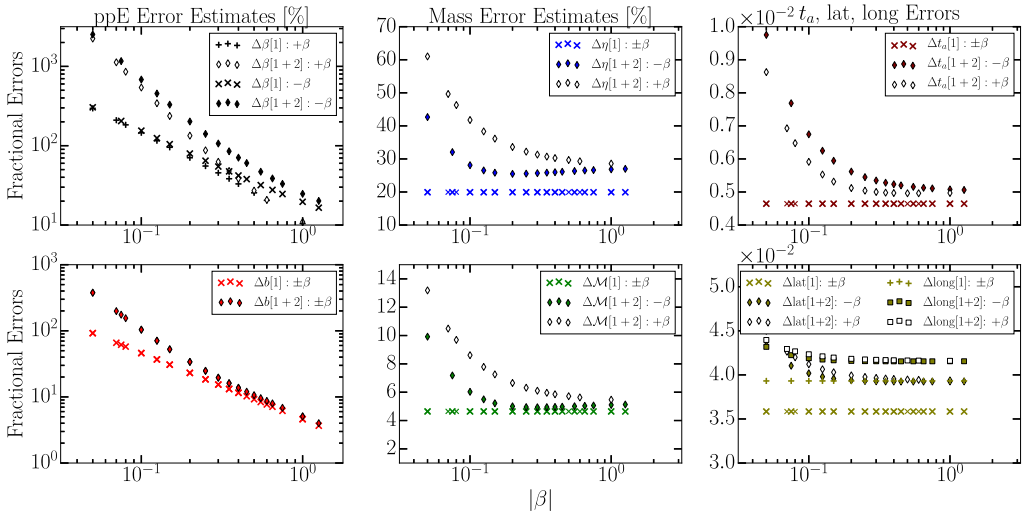

FIG. 4. Sky-averaged uncertainties for the equal-mass BBH 1:1 system for a PN-order 1.0 modification of the seven-dimensional parameter space (ppE parameters $\{\beta, b\}$ and physical parameters $\{\eta, \log \mathcal{M}, t_c, \text{lat}, \text{long}\}$). In the left column the top panel displays $\Delta\beta$ percent errors as a function of β (the sign of β provides different error estimates) and below that are Δb errors as a function of β (the sign of β does not play a role in these error estimates). In the middle and to the right are the physical parameters' errors, where the constraint of β primarily affects the second-order contributions. Enlarging the parameter space increases error estimates from those computed in Fig. 2 at PN order 1.0, thus weakening constraints on β. For negative β, the full-dimensional study states $\Delta\beta[1] = 100\%$ at $\beta = -0.16$ and $\Delta\beta[1+2] = 100\%$ at $\beta = -0.32$.

second-order contributions in b. If b is near distinguishable, $\Delta b[1+2] \lesssim 100\%$, $\Delta\beta[1+2]$ are much larger than $\Delta\beta[1]$. Only when $\Delta b[1+2] \lesssim 10\%$ do $\Delta\beta[1]$ and $\Delta\beta[1+2]$ converge to similar estimates. Simulations producing the results of Figs. 2 and 3 used both $\pm\beta$ values and the skewed representation of Fig. 1 is not apparent. Note that the range of β values, in which error bounds are $\lesssim 100\%$ (Figs. 2 and 3), are orders of magnitude smaller than the β-value ranges considered in previous studies based on Bayesian methods [18].

B. Full parameter space: Equal mass

The most realistic results come from the study of the largest resolvable parameter space. In this subsection, first- and second-order uncertainties $\Delta\vartheta^i$ of a full seven-dimensional parameter space are calculated for the equal-mass BBH 1:1 system, where $\vartheta = \{\theta_{\text{ppE}}, \theta_{\text{phys}}\}$. Here b is fixed to induce a PN-order 1.0 modification ($b = -3$). Such corrections simulate effects produced by modifying the GW dispersion relation [8,25]. Unlike the two-dimensional cases, the errors (first- and second-order) are effected by the sign of β, where sky-averaged errors for the ppE parameter pair (β, b) are displayed in the left column of Fig. 4. Errors of physical parameters affected by varying β are depicted in the middle and right column of Fig. 4. The skewed behavior of $\pm\beta$ results are representative of fitting factor results of Fig. 1.

For β the first-order errors are not at a constant slope. $\Delta\beta[1]$ approximately follows a linear relationship: $\Delta\beta[1] \approx 0.046|\beta| + 0.15$, for negative β. Here a 100% threshold error occurs at $\beta = -0.16$ for $\Delta\beta[1]$ and at $\beta = -0.32$ for $\Delta\beta[1+2]$. In this more realistic scenario, it can

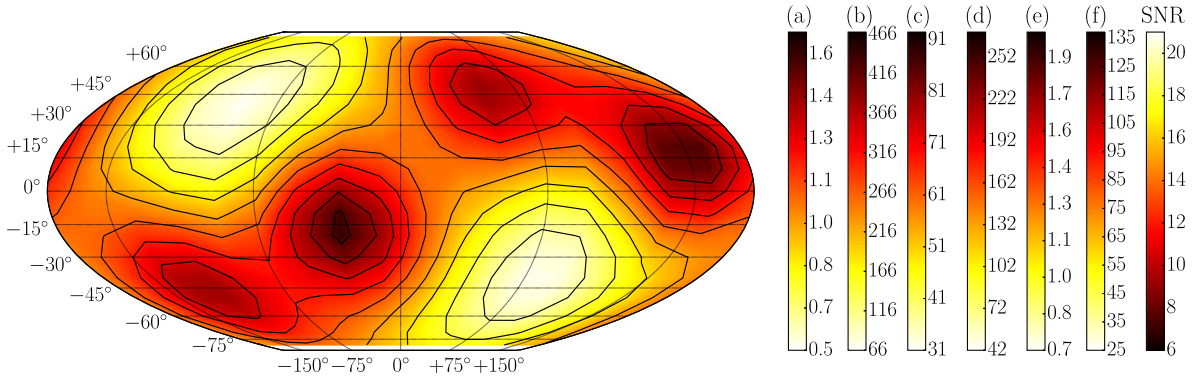

FIG. 5. Sky distribution of error estimates. Color bars represent the range of ppE quantities labeled (a), (b), …, (f) in Table II. This demonstrates the correlation of the SNR and ppE error estimation over the sky. See text for discussion.

TABLE II. Maxima and minima of estimates depicted in the sky-map plot (Fig. 5) for respective β-values of Fig. 4. Errors are the smallest for $\rho_{\max} = 20.8$ and largest for $\rho_{\min} = 7.0$. Terms labeled with (a), (b), …, (f) correspond to the respective color bars in Fig. 5. Values are chosen because they offer the most insight.

ppE β-value	Error estimations	$\rho_{\max} = 20.8$	$\rho_{\min} = 7.0$
−0.25			
(a)	$\Delta b[2]/\Delta b[1]$	0.55	1.67
	$\Delta b[1]$	12.1 (%)	36.2 (%)
	$\Delta b[1+2]$	13.8 (%)	70.5 (%)
	$\Delta\beta[2]/\Delta\beta[1]$	1.19	3.57
	$\Delta\beta[1]$	42.7 (%)	126.4 (%)
(b)	$\Delta\beta[1+2]$	66.4 (%)	468.7 (%)
−0.35			
	$\Delta b[2]/\Delta b[1]$	0.43	1.28
	$\Delta b[1]$	8.7 (%)	25.8 (%)
	$\Delta b[1+2]$	9.4 (%)	42.0 (%)
	$\Delta\beta[2]/\Delta\beta[1]$	0.91	2.72
(c)	$\Delta\beta[1]$	31.4 (%)	92.9 (%)
(d)	$\Delta\beta[1+2]$	42.4 (%)	269.1 (%)
−0.55			
	$\Delta b[2]/\Delta b[1]$	0.32	0.99
	$\Delta b[1]$	5.5 (%)	16.4 (%)
	$\Delta b[1+2]$	5.8 (%)	23.2 (%)
(e)	$\Delta\beta[2]/\Delta\beta[1]$	0.65	1.96
	$\Delta\beta[1]$	21.1 (%)	62.4 (%)
(f)	$\Delta\beta[1+2]$	25.2 (%)	137.3 (%)

be seen that for extremely small β values b falls within its own uncertainty. Yet, analogous to the two-parameter space, a 100% error in $\Delta b[1+2]$ requires large errors in $\Delta\beta[1+2]$. Furthermore, error estimates are at least an order of magnitude larger. Another aspect of considering a full-dimensional parameter space are the additional error trends imparted on physical parameters (masses, arrival time, etc.) when β is varied; see the middle and right column of Fig. 4.

The sky distributions of the errors and the SNR are shown in Fig. 5. Table II catalogs this for $-\beta = 0.25, 0.35, 0.55$. This SNR dependence is similar to intrinsic parameters for GWs. The β values, being a PN-order 1.0 correction characterizing massive graviton dispersion tests, are chosen for the following reasons:

(1) At $\beta = -0.25$, Fig. 4 identifies the conditions: $\Delta b[2]/\Delta b[1] \approx 1$ with $\Delta\beta[1] < 100\% < \Delta\beta[1+2]$. Sky averages are performed before computing the ratios. In SNR $\gtrsim 15$, we have $\Delta b[2]/\Delta b[1] \lesssim 1$, as seen in (a). (b) displays $\Delta\beta[1+2]$, which ranges from 66.4% to 468.7%. $\Delta\beta[2]$ dominates the error budget.

(2) For $\beta = -0.35$, sky-averaged $\Delta\beta[1] < \Delta\beta[1+2] \approx 100\%$. Although $\Delta b[2]/\Delta b[1] > 1$, in limited portions of the sky, the ratio never exceeds 1.3 with a maximum of $\Delta b[1+2] = 42.0\%$. There is a strong increase in $\Delta\beta[1+2]$ from $\Delta\beta[1]$ in low SNRs. The majority of the sky is dominated by second-order terms, with $\Delta\beta[2]/\Delta\beta[1]$ ranging from 0.91 to 2.72.

(3) $\beta = -0.55$ is where we calculate the sky-averaged ratio $\Delta\beta[2]/\Delta\beta[1] \approx 1$ with $\Delta\beta[1] < \Delta\beta[1+2] < 100\%$. Here a larger portion of the sky has ratio $\Delta\beta[2]/\Delta\beta[1] < 1$ as shown in (e). A majority (but not all) of the sky map has total error falling below 100% after the inclusion of second orders with sky-averaged error at $\Delta\beta[1+2] \approx 47\%$.

From the known dependence on ρ, quantities displayed in Fig. 5 and Table II can be easily rederived for higher or lower SNRs.

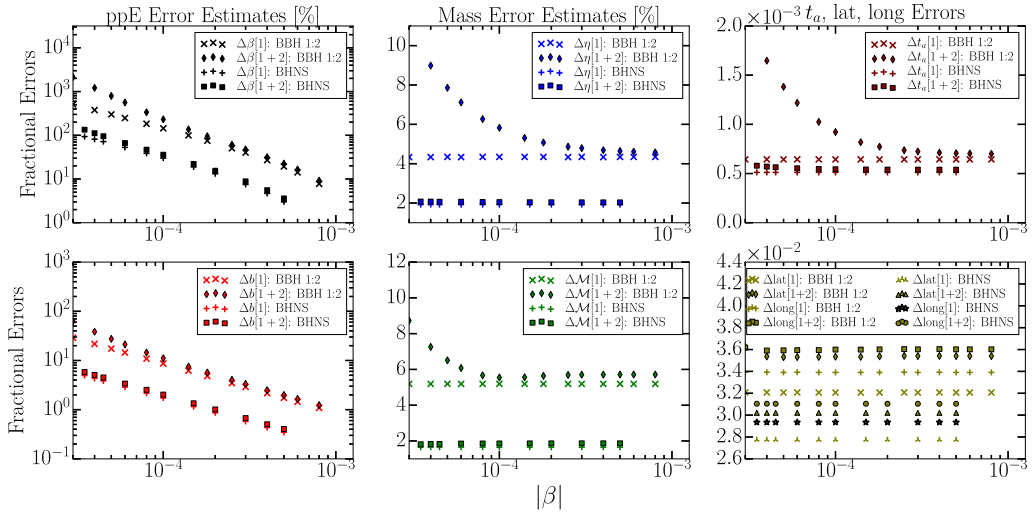

FIG. 6. Sky-averaged error estimates for the BBH 1:2 and BHNS system. The left column represents calculations of the ppE parameter errors $(\Delta\beta, \Delta b)$ for negative β-values, the center column shows the mass errors $(\Delta\eta, \Delta\mathcal{M})$, and the far right column shows the arrival time Δt_a and latitude-longitude $(\Delta\text{lat}, \Delta\text{long})$ error estimates. Here latitude-longitude error estimates are not affected by β variation, as was previously presented in the equal-mass system. This study states that $\Delta\beta_{\text{BBH1:2}}[1+2] = 95.2\%$ at $\beta_{\text{BBH1:2}} = -1.8 \times 10^{-4}$ and $\Delta\beta_{\text{BHNS}}[1+2] = 95.3\%$ at $\beta_{\text{BHNS}} = -4.5 \times 10^{-5}$.

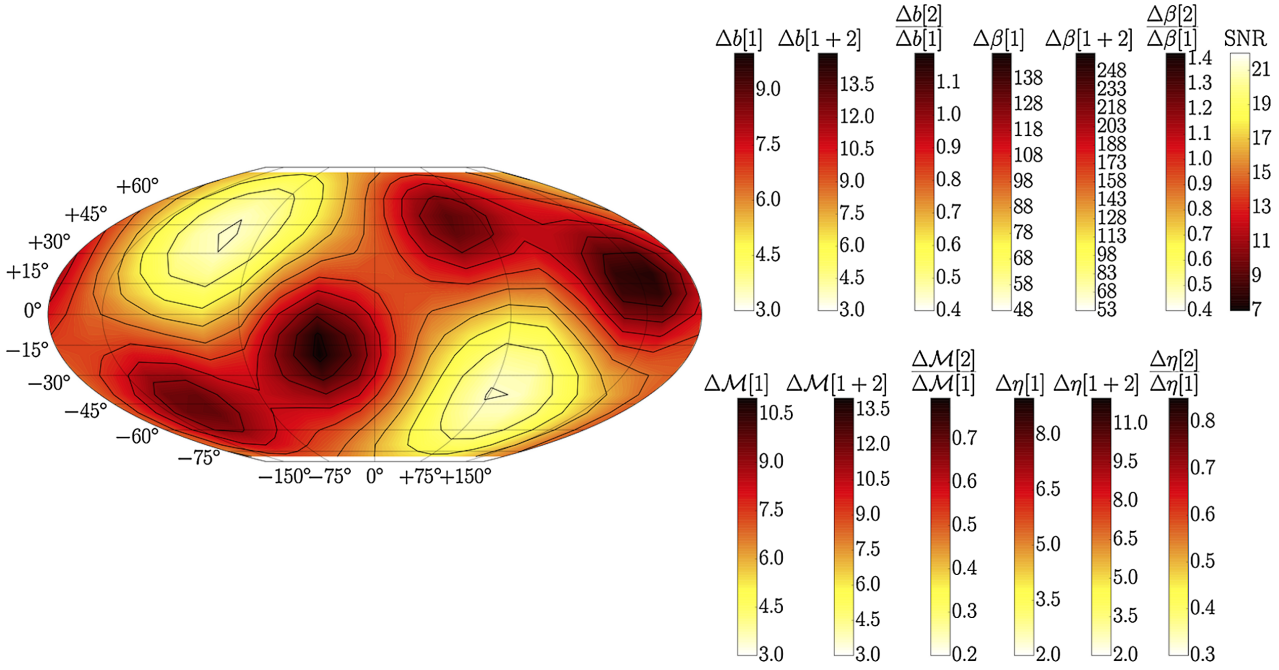

FIG. 7. Sky-map error estimates of ppE parameters $\Delta\beta$ and Δb and mass parameters $\Delta\eta$ and $\Delta\mathcal{M}$ for the unequal mass BBH 1:2 system. The top color bars for ppE parameters are for $\beta_{\mathrm{BBH1:2}} = -1.8 \times 10^{-4}$ and the mass parameters below that are for $\beta_{\mathrm{BBH1:2}} = -3.0 \times 10^{-4}$ of results in Fig. 6. The SNR color bar is valid for both error estimates. Sky-average estimates provide $\Delta\beta_{\mathrm{BBH1:2}}[1+2] = 95.2\%$ at $\beta_{\mathrm{BBH1:2}} = -1.8 \times 10^{-4}$ and $\Delta\beta_{\mathrm{BBH1:2}}[1+2] = 47.4\%$ at $\beta_{\mathrm{BBH1:2}} = -3.0 \times 10^{-4}$.

C. Full parameter space: Unequal mass

Here first- and second-order uncertainties $\Delta\vartheta^i$ of a full seven-dimensional parameter space are calculated for the BBH 1:2 and BHNS system. In this case a weak-field $b = -7$ modification is induced, which in our context mimics the nonspinning, even-parity sector of QMG and can include specifics like EDGB gravity. Inclusion of QMG modifications is due to β being resolvable by nonzero mass differences at this PN order. These modifications manifest through modification of the energy flux as $\beta \propto \zeta_3(1-4\eta)$ [39] and the BHNS binary can also test examples of dipole gravitational radiation, like Brans-Dicke (BD).

Error bounds are presented in Fig. 6. The overall trend of this system's estimates is similar to the results of the equal-mass BBH 1:1 of the previous subsection, with a few exceptions. The first is that the separation between errors $\Delta\beta[1]$, $\Delta b[1]$ and $\Delta\beta[1+2]$, $\Delta b[1+2]$ is not as great as with the PN-order 1.0 modification. In comparison to the previous subsection, the chirp mass errors $\Delta\mathcal{M}$ are roughly the same, yet $\Delta\eta$ estimates are considerably less. Time of arrival errors Δt_a are also less and latitude-longitudinal estimates do not suffer from varying β at first and second order.

For the BBH 1:2 system sky contours of ppE and mass error estimates at, respectively, $|\beta| = 1.8 \times 10^{-4}$ and $|\beta| = 3.0 \times 10^{-4}$ are displayed in Fig. 7. In Fig. 7, the mass error estimates (bottom color bars) are plotted since this β-value produces a sky-averaged estimate $\Delta\beta[1+2] < 100\%$, with second-order effects in the mass estimates making notable contributions (see Fig. 6). We observe that in such a context second-order effects do not dominate the error budget of $\Delta\eta$ and $\Delta\mathcal{M}$ in this sky grid. In low-SNR regions, $\Delta\eta[2]/\Delta\eta[1]$ and $\Delta\mathcal{M}[2]/\Delta\mathcal{M}[1]$ are near unity. In these same low-SNR regimes $\Delta\beta[2]/\Delta\beta[1] > 1$ and $\Delta\beta[1+2] > 100\%$, which demonstrates the sky-grid SNR relation to errors accrued on physical parameters due to large error estimates of ppE parameters.

Figure 7 also represents a second set of contours generated for $|\beta| = 1.8 \times 10^{-4}$ modifications. The top color bars are representative of ppE parameter error estimates $(\Delta\beta, \Delta b)$ valid for this choice of β. Contours are plotted at this β-value since this simulates the condition that $\Delta\beta[1+2] \approx 100\%$ with $\Delta\beta[1] < 100\%$. Again we observe the volatility in $\Delta\beta[1+2]$ estimates, ranging from 53% to about 250% while remaining strongly correlated to the SNR. One notable feature of this plot is that ratios $\Delta b[2]/\Delta b[1]$ and $\Delta\beta[2]/\Delta\beta[1]$ are relatively close to each other, being approximately equal to each other in regions of high SNR. This is in contrast to the equal-mass study of the previous subsection and demonstrates the small separation in $\Delta\beta[1]$ and $\Delta\beta[1+2]$ estimates depicted in the left column of Fig. 6, which allows the ratio $\Delta b[2]/\Delta b[1]$ to be comparable to $\Delta\beta[2]/\Delta\beta[1]$. Relations between these quantities depicted in Fig. 7 can be compared to the extrema of the equal-mass BBH system of PN-order 1.0 modifications cataloged in Table II. Similar results come from the BHNS system.

In order to check that the Fisher information matrix did not become singular we systematically explored its

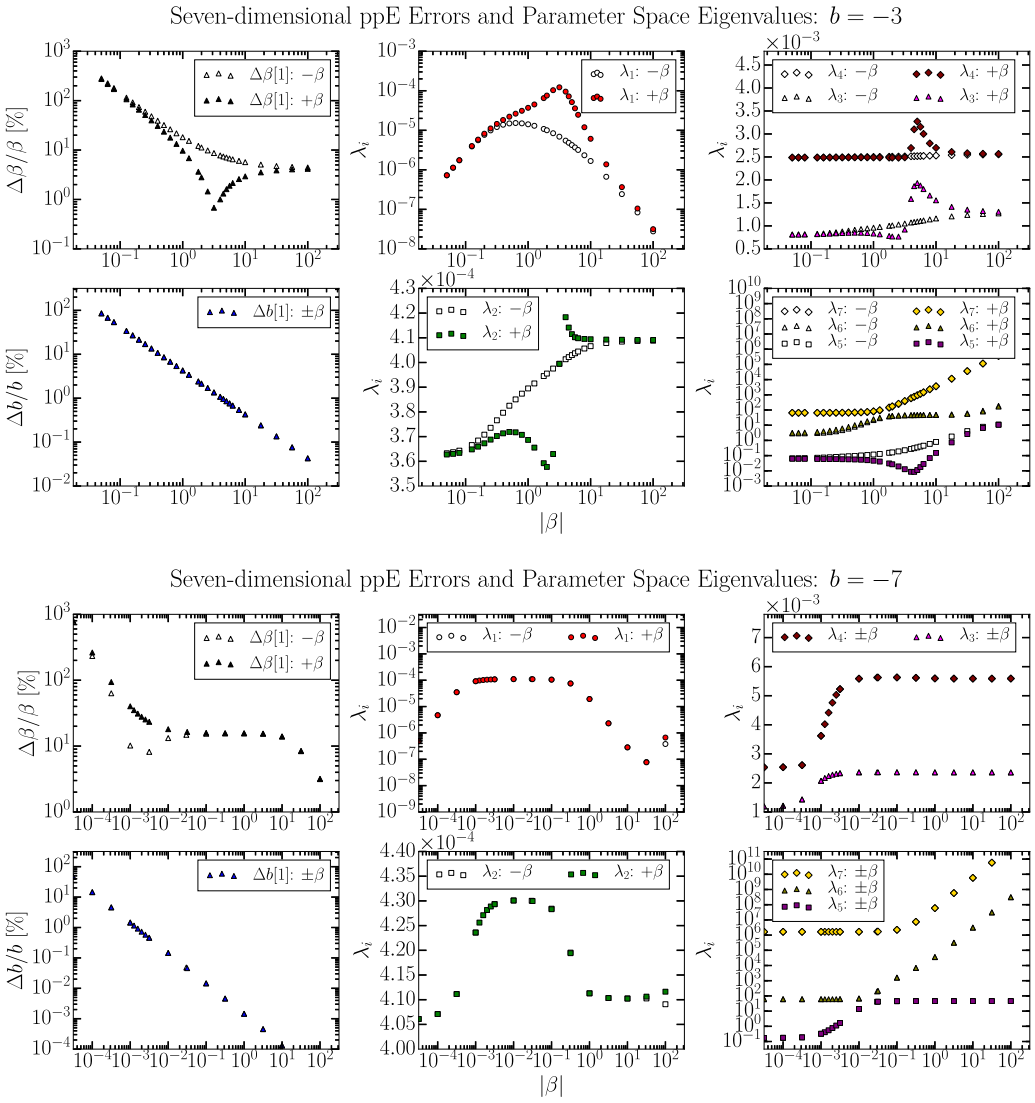

FIG. 8. First-order errors (left panels) and eigenvalues (center and right panels) of the Fisher matrix when computations are extended to the seven-dimensional parameter space.

eigenvalues. For example Fig. 8 shows scenarios in which the Fisher matrix becomes singular for the seven-dimensional study. These values of β were avoided in this analysis.

D. Application to explicit alternative theories

Since the modification considered in Sec. III B occurs at PN order 1.0 in the phase, an analysis can be done from these results for the massive graviton model. Progression of sky-averaged errors for $\Delta\beta[1+2]$, calculated from negative β-values, of Fig. 4 imposes a constraint of $|\beta_{\rm MG}| \leq 0.31$. Existing constraints are $|\beta_{\rm MG,static}| \leq 0.37$ and $|\beta_{\rm MG,GW}| \leq 2.89 \times 10^{-2}$, based on current static and dynamical (from GW150914 event) bounds on λ_g (see Sec. II A) computed from the BBH 1:1 system at 1100 Mpc. This asymptotic approach thus produces an additional 16.2% constraint on existing static bounds at 1σ. When including second-order terms in error estimation the constraints on λ_g have a fractional increase of 30% from the first-order Fisher matrix approach as calculated in this paper. Given these results, further constraints on the graviton wavelength λ_g may be possible, even with second-order error terms accounted for in the low-SNR limit of the inspiral stage only. From calculated results the sky-averaged feasible bounds are displayed in Table III.

Bayesian assessments in the ppE framework of unequal mass systems (of 1:2 and 1:3 ratios) with SNR of 20 put constraints at $\lambda_g > 8.8 \times 10^{12}$ km [18]. Other Bayesian studies also conclude that advanced detectors would generally not favor a MG theory over that of GR when λ_g is larger than the most stringent static bounds [19]. From the TIGER method implemented in the testing GR analysis of GW150914, constraints are at $\lambda_g > 10^{13}$ km, when the full inspiral-merger-ringdown signal is used (total SNR of

$\rho \sim 24$) [6]. In this respect, our errors impart a more conservative approach to error estimation that suggests that constraints may still be improved.

An application of seven-dimensional results presented in Sec. III C for the BBH 1:2 can also be made. This $b = -7$ modification has $\beta_{\rm QMG} \propto \zeta_3(1-4\eta)$. In this context the constraint parameter is $\zeta_3 = \xi_3 M^{-4}$ in the nonspinning, even-parity sector of QMG, where $\xi_3 = 16\pi\alpha^2_{\rm EDGB}$ in EDGB gravity [39]. For the BBH 1:2 system Fig. 6 presents $\Delta\beta[1] = 99.7\%$ at $|\beta| = 1.4\times10^{-4}$ and $\Delta\beta[1+2] = 95.2\%$ at $|\beta| = 1.8\times10^{-4}$. These computations translate to respective inputs in Table III for ξ_3 and $\alpha_{\rm EDGB}$. The strongest suggested constraints have, in terms of the EDGB parameter, $|\alpha_{\rm EDGB}|^{1/2} < 1.9$ km and $|\alpha_{\rm EDGB}|^{1/2} < 9.8$ km [40,53]. In weak-field tests the Cassini spacecraft has provided $|\alpha_{\rm EDGB}|^{1/2} < 8.9\times10^6$ km (i.e., $\xi_3^{1/4} < 2.4\times10^7$ km) [51]. Bayesian results estimate $\xi_3^{1/4} \lesssim 11$ km (or $|\alpha_{\rm EDGB}|^{1/2} \lesssim 4$ km) at a SNR of 20 [39] which is quoted in Ref. [8] as $\xi_3^{1/4} \lesssim 20$ km for a SNR of 10.

Similar application to QMG and EDGB theories can be done with results of the BHNS system. These constraints are also presented in Table III and are more stringent than the BBH 1:2 system. With BHNS systems, Brans-Dicke can be investigated through $\beta_{\rm BD} \propto (s_1 - s_2)^2\omega_{\rm BD}^{-1}$, where the constraint parameter is $\omega_{\rm BD}$ with $s_{\rm BH} = 0.5$ for black holes and for neutron stars $0.2 \le s_{\rm NS} \le 0.3$ [41–44]. Figure 6 results indicate $\Delta\beta[1] = 95.3\%$ at $|\beta| = 4.5\times10^{-5}$ for the BHNS system. Thus, constraints result in $\omega_{\rm BD} \ge 1.14$ and $\omega_{\rm BD} \ge 0.51$ at $s_{\rm NS} = 0.2$ and $s_{\rm NS} = 0.3$, respectively. Results of the Cassini spacecraft have also established $\omega_{\rm BD} > 4\times10^4$ [52]. In Ref. [21] Fisher estimates placed constants of $\omega_{\rm BD} > 194$ for BHNS systems of similar masses.

IV. CONCLUSION

In this paper we implement a frequentist asymptotic expansion method to estimate error bounds on the set of ppE parameters modifying the phase of the inspiral part of low-SNR ($\rho \sim 15$–17) GW transients. Figure 9 provides a summary of the main results of this paper. The bound on the mean-squared error estimates from compact binaries studied is shown. Each mark represents the boundary of the (β, b)-parameter space where the minimum mean-squared error estimates are 100%, with β-values below each b-value > 100% and therefore not resolvable. Previous Bayesian studies correspond to the range of exponential ppE parameters, $-11 \le b \le 2$, as compared to the Fig. 9 summary. The fact that for the massive graviton case ($b = -3$) our approach here, which is a more realistic lower limit of the Cramér-Rao lower bound for early detections, rules out results that were allowed by a Bayesian study [18] seems to indicate the need for a careful evaluation of the role of the priors.

Results of the higher-order asymptotic analysis of the frequentist approach to error estimation state that further constraints can be imposed on existing non-GR theories with the study of the seven-dimensional parameter space (see Table III). This approach does not involve the use of priors. Here the graviton wavelength can be constrained by an additional 16.2% as compared to current static bounds [50]. Yet, these projected constraints do not further bound the graviton wavelength when compared to Bayesian estimates or values imposed by GW150914 [6]. Note that although GW150914 provides a constraint of $\lambda_g > 10^{13}$ km, our result holds for a lower SNR of the inspiral stage only.

TABLE III. Seven-dimensional study of the BBH 1:1, 1:2, and BHNS systems with feasible constraints, i.e., computed MSE $\lesssim 100\%$. The first considers PN-order 1.0 modifications and the latter two consider $b = -7$ modifications. Included are the graviton wavelength (or generic Lorentz-violating) dispersion modification and nonspinning, even-parity sector models of QMG (EDGB parameter included). The Brans-Dicke constraint depends on sensitivity parameter $0.2 \le s_{\rm NS} \le 0.3$.

Distinguishability constraint ($\lesssim$100% error)	
$\lambda_{g,\rm LV} > 3.04\times10^{12}$ km	(BBH 1:1)
$\xi_3^{1/4} < 7.17$ km	(BBH 1:2)
$\lvert\alpha_{\rm EDGB}\rvert^{1/2} < 2.69$ km	(BBH 1:2)
$\xi_3^{1/4} < 9.45$ km	(BHNS)
$\lvert\alpha_{\rm EDGB}\rvert^{1/2} < 3.55$ km	(BHNS)
$\omega_{\rm BD} > 12.7(s_{\rm NS} - 0.5)^2$	(BHNS)

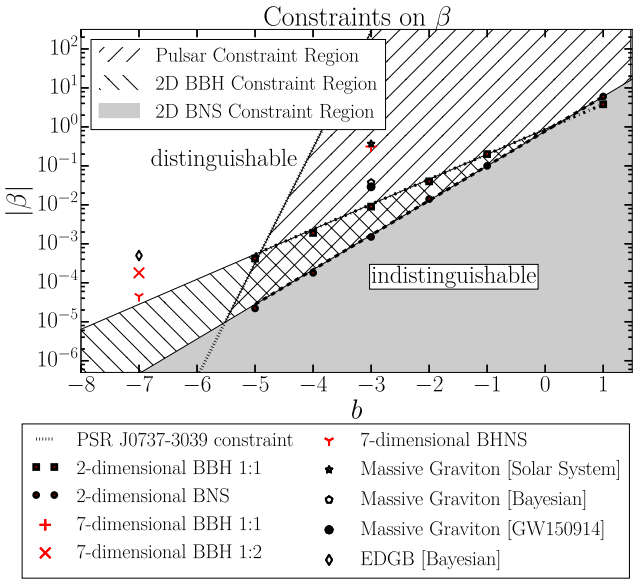

FIG. 9. Constraints on ppE parameters (β, b). Alongside frequentist mean-squared error $\lesssim$100% estimates are constraints imposed by Bayesian estimates [18], solar system tests [50], binary pulsar measurements [37,38], and the GW150914 event [6]. Regions below each mark/line are where violations cannot be detected based on each respective study. The GR-limit is $\beta = 0$. Our frequentist two-dimensional study considers ppE parameter space (β, b), while seven-dimensional studies include physical parameters (masses, etc.). See text for discussion.

Further studies present the scenario for the weak-field $b = -7$ modification, which can include QMG (or specifically EDGB gravity) and Brans-Dicke type modifications (Fig. 6). For the nonspinning, even-party sector of QMG, bounds suggest further constraints are possible as compared to current bounds placed by Bayesian estimates and Cassini constraints. Furthermore, error estimates for modifications at both PN order 1.0 and the $b = -7$ weak field follow similar sky-map contours, which are correlated to the SNR patterns (see Figs. 5 and 7).

General results show that for successively higher PN-order modifications, set by b, the separation between first- and second-order errors increases (see Figs. 2 and 3). Such an effect percolates to the seven-dimensional study. Error bounds also increase as the parameter space is enlarged, where the two-dimensional studies provide overly optimistic error bounds. As constraints on β become tighter in the seven-dimensional studies, the effects of second-order estimates also accrue on physical parameters, namely, η, $\mathcal{M}$, t_a, and latitude-longitude parameters (see Figs. 4 and 6). Finally, SNR increases translate error estimates as discussed in Ref. [11] (Fig. 2), so all results can be rescaled as a function of the SNR.

Calculations performed in this paper are for single detection scenarios. With multiple detections the presence of weak, but consistent, violations could be combined to make a stronger statement about error estimations. Such methods to *resolve* consistent signals were explored in a Bayesian framework in Ref. [16] and it is left for future studies in the frequentist framework. Furthermore, as waveform models advance, for both the inspiral and ppE framework, the application of our maximum likelihood estimator asymptotic expansion could be applied to spinning binaries or to waveforms that include the merger and ringdown phases. This will add insight into additional modified theories mappable into the ppE framework.

ACKNOWLEDGMENTS

The authors would like to thank S. Vitale, T. G. F. Li, A. J. Weinstein, W. D. Pozzo, L. Stein, and K. Yagi for useful discussion and comments. R. Tso is supported by the National Science Foundation Graduate Research Fellowship Program under Grant No. DGE-1144469, the Ford Foundation Predoctoral Fellowship, and the Gates Foundation.

APPENDIX: NOTATION AND NETWORK SIGNAL

Masses of each compact body are labeled as $m_{1,2}$, the total mass being $M = m_1 + m_2$ with $\nu = (\pi M f)^{1/3}$ and $\eta = m_1 m_2/M^2$ as the reduced mass frequency and symmetric mass ratio, respectively. The usual chirp mass is $\mathcal{M} = \eta^{3/5} M$. Geometrized units ($G = c = 1$) are also employed [58]. Terms labeled with I indicate a particular quantity for that Ith detector; e.g., s^I is a signal received at some Ith detector, ρ^I is a detector-dependent SNR, etc. Finally, the detectors considered are those for Advanced LIGO and Advanced Virgo, so we have $I = H, L, V$ for the respective advanced interferometers in Hanford, USA; Livingston, USA; and Cascina, Italy. Quantities summed over I indicate the total network contribution of that term, e.g., network SNR and network Fisher matrix. Apart from the units employed, the notation follows that of Ref. [36].

To discuss some of the terms appearing in (1.1): τ_I is a time lag parameter accounting for the delay in the waveform's propagation from the Ith detector frame (IDF) to some fiducial frame (FF),[3] with μ^I and Φ_0^I being coefficients that depend on the inclination angle ϵ of the binary system and the generalized antenna patterns $\mathcal{F}^I_{+,\times}$ of each detector. These are represented by

$$\tau_I = \hat{\mathbf{n}} \cdot (\mathbf{r}_I - \mathbf{r}_{FF}), \tag{A1}$$

$$\mu^I = \left(\left(\frac{1}{2} \mathcal{F}^I_+ (1 + \cos^2 \epsilon) \right)^2 + (\mathcal{F}^I_\times \cos \epsilon)^2 \right)^{1/2}, \tag{A2}$$

$$\Phi_0^I = \arctan \frac{2\mathcal{F}^I_\times \cos \epsilon}{\mathcal{F}^I_+ (1 + \cos^2 \epsilon)}, \tag{A3}$$

with $\hat{\mathbf{n}}$ the direction of travel of the waveform; $\mathbf{r}_I$ the distance to the Ith detector (i.e., the IDF origin); and $\mathbf{r}_{FF}$ the distance to the FF origin. The construction of a frame of common origin improves the feasibility of and efficiency displayed in calculations of quantities in particular frames. The notion of a common origin between the frames is valid since approximate measures[4] allow the origins of the coordinate systems to coincide. With respect to Ref. [11] the frames are established as the already mentioned IDF and FF, with a third frame called the wave frame (WF).[5] In producing calculable quantities the frames are then fixed to values of that in the Earth frame (EF).

Since the origins of the frames coincide, transformation between the frames is feasible through simple Eulerian angles with the usual ZXZ convention [59]. From this, a set of Euler angles (ϕ, θ, ψ) converts a quantity from the FF into the WF and another set $(\alpha^I, \beta^I, \gamma^I)$ converts from the FF into the IDF through the usual rotation matrices. Here angle ψ is the polarization angle. A variety of relations can be uncovered after defining a few new angles. Let angle pairs (Φ, Θ) and (long, lat) describe the source's location in the sky (the former being in spherical coordinates and the latter in longitude-latitude coordinates); let (Ξ, ζ) be defined from projections of $\hat{\mathbf{n}}$ onto the FF's axis; define angles (Ω^I, Υ^I) so

[3]FF is the frame in which the origins are referenced to coincide.

[4]Through reasonable assumption of zero curvature over the course of the GW's propagation and introduction of time lag τ_I.

[5]Determined through the GW's direction of travel and orthonormal WF unit vectors along its axis, where dominant harmonic polarizations in the waveform are assumed.

that they prescribe the location of the Ith detector with respect to the FF; and allow angle Δ^I to span the region between the first detector arm (in the IDF) and the local northern direction. These relations are summarized as follows:

$$\phi = \Phi - \frac{\pi}{2} = \text{long} - \frac{\pi}{2} = \Xi + \frac{\pi}{2}$$
$$\theta = \pi - \Theta = \frac{\pi}{2} + \text{lat} = \zeta \tag{A4}$$

and

$$\alpha^I = \Omega^I + \frac{\pi}{2}, \qquad \beta^I = \frac{\pi}{2} - \Upsilon^I, \qquad \gamma^I = \Delta^I + \frac{\pi}{2}. \tag{A5}$$

Formulation of $\mathcal{F}^I_{+,\times}$ into a symmetric-trace-free base has been performed, with respect to the Eulerian angle dependence, and what surfaces in the frequency-represented signal are the two generalized antenna patterns:

$$\mathcal{F}^I_+ = \frac{1}{2}(T_{2s}(\alpha^I,\beta^I,\gamma^I) + T_{-2s}(\alpha^I,\beta^I,\gamma^I)) \times (T^*_{2s}(\phi,\theta,\psi) + T^*_{-2s}(\phi,\theta,\psi)) \tag{A6}$$

$$\mathcal{F}^I_\times = \frac{i}{2}(T_{2s}(\alpha^I,\beta^I,\gamma^I) + T_{-2s}(\alpha^I,\beta^I,\gamma^I)) \times (T^*_{2s}(\phi,\theta,\psi) - T^*_{-2s}(\phi,\theta,\psi)) \tag{A7}$$

where T_{mn} are second-order Gel'fand functions (T^*_{mn} being their complex conjugates). Function statements, such as $f(\alpha^I,\beta^I,\gamma^I)$ and $g(\phi,\theta,\psi)$, represent their dependencies on Euler angle rotations from $FF \to IDF$ and $FF \to WF$, respectively. See Ref. [11] for exemplary calculations. Note that an auxiliary ppE template has been developed that considers extra polarizations of waveforms produced in non-GR gravity, incorporating additional propagating degrees of freedom in the ppE framework [31]. Although it is of interest to measure extra polarizations expected in a variety of alternative theories of gravity, these extra modes lead to more complex models. For initial analysis of modified gravity through the asymptotic maximum likelihood estimator approach, a ppE template with only the standard two propagating modes is considered both sufficient and satisfactory for now. Reference [60] investigated methods to test non-GR polarizations via continuous waveforms from asymmetric pulsars.

[1] G. M. Hardy (LIGO Scientific Collaboration), Classical Quantum Gravity **27**, 084006 (2010).
[2] https://www.advancedligo.mit.edu.
[3] https://wwwcascina.virgo.infn.it/advirgo.
[4] B. P. Abbott *et al.*, Phys. Rev. Lett. **116**, 061102 (2016).
[5] C. M. Will, Living Rev. Relativ. **9**, 3 (2006).
[6] B. P. Abbott *et al.*, arXiv:1602.03841.
[7] J. R. Gair, M. Vallisneri, S. L. Larson, and J. G. Baker, Living Rev. Relativ. **16**, 7 (2013).
[8] N. Yunes and X. Siemens, Living Rev. Relativ. **16**, 9 (2013).
[9] S. Vitale and M. Zanolin, Phys. Rev. D **82**, 124065 (2010).
[10] M. Zanolin, S. Vitale, and N. Makris, Phys. Rev. D **81**, 124048 (2010).
[11] S. Vitale and M. Zanolin, Phys. Rev. D **84**, 104020 (2011).
[12] N. Yunes and F. Pretorius, Phys. Rev. D **80**, 122003 (2009).
[13] K. G. Arun, B. R. Iyer, M. S. S. Qusailah, and B. S. Sathyaprakash, Classical Quantum Gravity **23**, L37 (2006).
[14] K. G. Arun, B. R. Iyer, M. S. S. Qusailah, and B. S. Sathyaprakash, Phys. Rev. D **74**, 024006 (2006).
[15] C. K. Mishra, K. G. Arun, B. R. Iyer, and B. S. Sathyaprakash, Phys. Rev. D **82**, 064010 (2010).
[16] T. G. F. Li, W. Del Pozzo, S. Vitale, C. VanDenBroeck, M. Agathos, J. Veitch, K. Grover, T. Sidery, R. Sturani, and A. Vecchio, Phys. Rev. D **85**, 082003 (2012).
[17] T. G. F. Li, W. D. Pozzo, S. Vitale, C. V. D. Broeck, M. Agathos, J. Veitch, K. Grover, T. Sidery, R. Sturani, and A. Vecchio, J. Phys. Conf. Ser. **363**, 012028 (2012).
[18] N. Cornish, L. Sampson, N. Yunes, and F. Pretorius, Phys. Rev. D **84**, 062003 (2011).
[19] W. Del Pozzo, J. Veitch, and A. Vecchio, Phys. Rev. D **83**, 082002 (2011).
[20] D. S. Sivia and J. Skilling, in *Data Analysis: A Bayesian Tutorial*, 2nd ed. (Oxford University Press, New York, 2006).
[21] C. M. Will, Phys. Rev. D **50**, 6058 (1994).
[22] C. M. Will, Phys. Rev. D **57**, 2061 (1998).
[23] A. Pai and K. G. Arun, Classical Quantum Gravity **26**, 155002 (2009).
[24] D. Keppel and P. Ajith, Phys. Rev. D **82**, 122001 (2010).
[25] S. Mirshekari, N. Yunes, and C. M. Will, Phys. Rev. D **85**, 024041 (2012).
[26] A. Buonanno, B. R. Iyer, E. Ochsner, Y. Pan, and B. S. Sathyaprakash, Phys. Rev. D **80**, 084043 (2009).
[27] K. G. Arun, B. R. Iyer, B. S. Sathyaprakash, and Pranesh A. Sundararajan, Phys. Rev. D **71**, 084008 (2005); **72**, 069903 (E) (2005).
[28] T. A. Apostolatos, Phys. Rev. D **52**, 605 (1995).
[29] B. S. Sathyaprakash and S. V. Dhurandhar, Phys. Rev. D **44**, 3819 (1991).
[30] C. M. Bender and S. A. Orszag, in *Advanced Mathematical Methods for Scientists and Engineers I, Asymptotic Methods and Perturbation Theory* (Springer, New York, 1999).
[31] K. Chatziioannou, N. Yunes, and N. Cornish, Phys. Rev. D **86**, 022004 (2012).
[32] M. Vallisneri and N. Yunes, Phys. Rev. D **87**, 102002 (2013).
[33] Advanced LIGO anticipated sensitivity curves, LIGO Document Report No. T0900288-v3.

[34] F. Acernese *et al.* (VIRGO Collaboration), Classical Quantum Gravity **32**, 024001 (2015).
[35] M. Vallisneri, Phys. Rev. D **77**, 042001 (2008).
[36] M. Maggiore, in *Gravitational Waves* (Oxford University Press, New York, 2007), Vol. 1.
[37] N. Yunes and S. A. Hughes, Phys. Rev. D **82**, 082002 (2010).
[38] A. G. Lyne *et al.*, Science **303**, 1153 (2004).
[39] K. Yagi, L. C. Stein, N. Yunes, and T. Tanaka, Phys. Rev. D **85**, 064022 (2012).
[40] K. Yagi, Phys. Rev. D **86**, 081504 (2012).
[41] J. Healy, T. Bode, R. Haas, E. Pazos, P. Laguna, D. M. Shoemaker, and N. Yunes, Classical Quantum Gravity **29**, 232002 (2012).
[42] S. Mirshekari and C. M. Will, Phys. Rev. D **87**, 084070 (2013).
[43] N. Yunes, P. Pani, and V. Cardoso, Phys. Rev. D **85**, 102003 (2012).
[44] H. W. Zaglauer, Astrophys. J. **393**, 685 (1992).
[45] K. Yagi, N. Yunes, and T. Tanaka, Phys. Rev. Lett. **109**, 251105 (2012).
[46] J. Beringer *et al.* (Particle Data Group Collaboration), Phys. Rev. D **86**, 010001 (2012).
[47] D. Colladay and V. A. Kostelecký, Phys. Rev. D **58**, 116002 (1998).
[48] V. A. Kostelecký, Phys. Rev. D **69**, 105009 (2004).
[49] V. A. Kostelecký and J. D. Tasson, Phys. Lett. B **749**, 551 (2015).
[50] E. Berti, J. Gair, and A. Sesana, Phys. Rev. D **84**, 101501 (2011).
[51] L. Amendola, C. Charmousis, and S. C. Davis, J. Cosmol. Astropart. Phys. 10 (2007) 004.
[52] B. Bertotti, L. Iess, and P. Tortora, Nature (London) **425**, 374 (2003).
[53] P. Pani, E. Berti, V. Cardoso, and J. Read, Phys. Rev. D **84**, 104035 (2011).
[54] N. Yunes, K. Yagi, and F. Pretorius, arXiv:1603.08955 [Phys. Rev. D (to be published)].
[55] V. A. Kostelecký and M. Mewes, Phys. Lett. B **757**, 510 (2016).
[56] B. Allen, arXiv:gr-qc/9607075.
[57] B. F. Schutz, Classical Quantum Gravity **28**, 125023 (2011).
[58] C. W. Misner, K. S. Thorne, and J. A. Wheeler, in *Gravitation* (W.H. Freeman, San Francisco, 1973).
[59] H. Goldstein, in *Classical Mechanics*, 2nd ed. (Addison-Wesley, Reading, MA, 1980).
[60] M. Isi, A. J. Weinstein, C. Mead, and M. Pitkin, Phys. Rev. D **91**, 082002 (2015).